line (PBS, pH = 7.4). This immobilization method provides a tight streptavidin layer with uniform density on gold for efficient binding of biotin. All of the nonspecific binding sites were blocked with bovine serum albumin (BSA). For detection experiments, the functionalized microcantilevers were exposed to target biotin concentrations (in PBS) of 100 fg/ml, 100 pg/ml, and 100 ng/ml.

MOSFET transistors were passivated with a thin coating of silicon nitride (30 nm), and electrical contacts were isolated for the binding measurements in the fluidic environment. The measured drain current (I_D) versus drain voltage (V_D) characteristics for the n-MOSFET–embedded transistor, at gate voltage $V_G = 5$ V, show a negligible change in I_D (Fig. 4A) when the streptavidin-immobilized gold microcantilevers are immersed in PBS. Microcantilever bending as a result of streptavidin-biotin binding leads to decreases in I_D as the concentration of biotin increases from 100 fg/ml to 100 ng/ml. The bending results from an increase in compressive stress, which in turn results from the repulsive electrostatic or steric intermolecular interactions (*2*–*6*) or from changes of the hydrophobicity of the surface (*1*–*6*). No drain current change was seen in SiN_x cantilevers with biotin, where no binding events occurred.

Similar experiments were performed for detection of goat antibodies [secondary immunoglobulin G (IgG)] by rabbit antibodies (primary IgG) with the embedded MOSFET. After the cleaning procedure, the MOSFET-embedded microcantilevers were first functionalized with DTSSP as a linker and then incubated overnight in rabbit IgG (0.1 mg/ml, Pierce) prepared in PBS for immobilization. BSA was again used as an agent to block nonspecific binding sites. The functionalized microcantilevers were exposed to goat antibody to rabbit IgG (0.1 mg/ml in PBS) for binding experiments.

The measured I_D versus V_D characteristics for $V_G = 5$ V (Fig. 4B) again showed no change in the drain current for the SiN_x cantilever and negligible change for the gold-coated cantilever with rabbit IgG immersed in PBS. When goat antibody to rabbit IgG (0.1 mg/ml) was introduced, a change in I_D of almost two orders of magnitude was observed, which is indicative of microcantilever bending as a result of antibody–secondary antibody binding. The SiN_x reference cantilever remained the same after injecting the target. The large change in I_D with time is shown in Fig. 4C; steady-state saturation is achieved when molecular and surface interactions are completed.

The MOSFET detection method offers a number of advantages over traditional piezoresistive or capacitive sensor elements because of its small size, high sensitivity, and uncomplicated current measurement as well as its full and seamless compatibility with direct monolithic integration for application-specific integrated circuits. Moreover, the small channel lengths of MOSFET devices provide more localized stress measurements. MOSFET-embedded microcantilever detection should allow for massively parallel on-chip signal sensing, multiplexing, and remote addressability via on-chip integration of radio-frequency elements as well as photovoltaics for local power supply.

References and Notes

1. R. Raiteri, M. Grattarola, H. J. Butt, P. Skladal, *Sens. Actuators B* **79**, 115 (2001).
2. G. Wu *et al.*, *Proc. Natl. Acad. Sci. U.S.A.* **98**, 1560 (2001).
3. G. Wu *et al.*, *Nat. Biotechnol.* **19**, 856 (2001).
4. J. Fritz *et al.*, *Science* **288**, 316 (2000).
5. N. V. Lavrik, M. J. Sepaniak, P. G. Datskos, *Rev. Sci. Instrum.* **75**, 2229 (2004).
6. M. Yue *et al.*, *J. Microelectromech. Syst.* **13**, 290 (2004).
7. A. Boisen, J. Thaysen, H. Jensenius, O. Hansen, *Ultramicroscopy* **82**, 11 (2000).
8. H. Jensenius *et al.*, *Appl. Phys. Lett.* **76**, 2615 (2000).
9. R. Marie, H. Jensenius, J. Thaysen, C. B. Christensen, A. Boisen, *Ultramicroscopy* **91**, 29 (2002).
10. S. C. Minne *et al.*, *Appl. Phys. Lett.* **72**, 2340 (1998).
11. S. C. Minne, S. R. Manalis, C. F. Quate, *Appl. Phys. Lett.* **67**, 3918 (1995).
12. D. R. Baselt, G. U. Lee, R. J. Colton, *J. Vac. Sci. Technol. B* **14**, 789 (1996).
13. D. R. Baselt, G. U. Lee, K. M. Hansen, L. A. Chrisey, R. J. Colton, *Proc. IEEE* **85**, 672 (1997).
14. C. L. Britton *et al.*, *Ultramicroscopy* **82**, 17 (2000).
15. A. Hamada, T. Furusawa, N. Saito, E. Takeda, *IEEE Trans. Electron Devices* **38**, 895 (1991).
16. R. C. Jaeger, J. C. Suhling, R. Ramani, A. T. Bradley, J. P. Xu, *IEEE J. Solid-State Circuits* **35**, 85 (2000).
17. Y. J. Yee, J. U. Bu, K. J. Chun, J. W. Lee, *J. Micromech. Microeng.* **10**, 350 (2000).
18. T. Akiyama *et al.*, *J. Vac. Sci. Technol. B* **18**, 2669 (2000).
19. D. Lange, C. Hagleitner, C. Herzog, O. Brand, H. Baltes, *Sens. Actuators A* **103**, 150 (2003).
20. T. Akiyama, U. Staufer, N. F. de Rooij, *Rev. Sci. Instrum.* **73**, 2643 (2002).
21. R. Bashir, A. Gupta, G. W. Neudeck, M. McElfresh, R. Gomez, *J. Micromech. Microeng.* **10**, 483 (2000).
22. C. Liu, *Foundations of MEMS* (Pearson Prentice Hall, Upper Saddle River, NJ, 2005).
23. V. Dessard, B. Iniguez, S. Adriaensen, D. Flandre, *IEEE Trans. Electron Devices* **49**, 1289 (2002).
24. A. Blaum, O. Pilloud, G. Scalea, J. Victory, F. Sischka, in *Proceedings of the 2001 International Conference on Microelectronic Test Structures* (IEEE, Piscataway, NJ, 2001), pp. 125–130.
25. P. A. Rasmussen, J. Thaysen, O. Hansen, S. C. Eriksen, A. Boisen, *Ultramicroscopy* **97**, 371 (2003).

26. Supported by NSF Electrical and Communications System grant ECS-0330410 and Defense Advanced Research Projects Agency grant F30602-01-2-0540. This work made use of the Microfabrication Applications Laboratory at the University of Illinois, Chicago, the Center for Nanophase Materials Science at Oak Ridge National Laboratory, and the NU*ANCE* center facilities at Northwestern University. We thank R. Lajos, H. Zeng, and A. Feinerman for process assistance and support; T. Thundat, D. Ramaya, K. Hansen, and I. Lee for assistance in immobilization of antibodies; and A. Srivastava for assistance in noise measurements.

Supporting Online Material

www.sciencemag.org/cgi/content/full/1122588/DC1
Materials and Methods
References

14 November 2005; accepted 20 January 2006
Published online 2 February 2006;
10.1126/science.1122588
Include this information when citing this paper.

Broadband Cavity Ringdown Spectroscopy for Sensitive and Rapid Molecular Detection

Michael J. Thorpe, Kevin D. Moll, R. Jason Jones, Benjamin Safdi, Jun Ye*

We demonstrate highly efficient cavity ringdown spectroscopy in which a broad-bandwidth optical frequency comb is coherently coupled to a high-finesse optical cavity that acts as the sample chamber. 125,000 optical comb components, each coupled into a specific longitudinal cavity mode, undergo ringdown decays when the cavity input is shut off. Sensitive intracavity absorption information is simultaneously available across 100 nanometers in the visible and near-infrared spectral regions. Real-time, quantitative measurements were made of the trace presence, the transition strengths and linewidths, and the population redistributions due to collisions and the temperature changes for molecules such as C_2H_2, O_2, H_2O, and NH_3.

The real-time detection of trace amounts of molecular species is needed for applications that range from detection of explosives or biologically hazardous materials to analysis of a patient's breath to monitor diseases such as renal failure (*1*) and cystic fibrosis (*2*). Spectroscopic systems capable of making the next generation of atomic and molecular measurements will require the following: (i) a large spectral bandwidth, allowing for the observation of the global energy level structure of many different atomic and molecular species; (ii) high spectral resolution for the identification and quantitative analysis of individual spectral features; (iii) high sensitivity for the detection of trace amounts of atoms or molecules and for the recovery of weak spectral features; and (iv) a fast spectral acquisition time, which takes advantage of high sensitivity, for the study of dynamics.

JILA, National Institute of Standards and Technology (NIST) and University of Colorado, and Department of Physics, University of Colorado, Boulder, CO 80309-0440, USA.

*To whom correspondence should be addressed. E-mail: ye@jila.colorado.edu

Unfortunately, the characteristics of a good spectroscopic system are often in competition with each other. For example, designing a system with a large spectral bandwidth and high resolution (or high sensitivity) requires some way of selecting a narrow spectral band from a broad-spectrum source. Thus, modern spectroscopic methods, which are designed to meet two or three of the desired system characteristics with excellent performance, will function poorly in the remaining areas. Single-pass absorption techniques, such as Fourier transform infrared (FTIR) (*3*) and wavelength agile methods (*4*), do an excellent job of providing large bandwidths (up to several hundreds of nanometers) and achieve remarkably fast acquisition times by recording entire spectra in microseconds. But these techniques offer sensitivities that are many orders of magnitude too low for applications involving trace detection or observation of weak spectral features. Both of these techniques can achieve high resolution but at the cost of prolonged spectral acquisition times or reduced spectral bandwidths.

Cavity-enhanced techniques, such as noise-immune, cavity-enhanced, optical heterodyne molecular spectroscopy (NICE-OHMS) (*5*, *6*) and cavity ringdown spectroscopy (CRDS) (*7*), offer incredibly high sensitivities (10^{-10} and beyond) at 1-s averaging time, and they can provide high resolution; however, they are generally limited to small spectral bandwidths (only a few nanometers). Newer approaches to cavity-enhanced spectroscopy have been directed at increasing the spectral bandwidth and reducing the acquisition time (*8*–*11*). Such efforts have demonstrated large bandwidths of up to 50 nm with an acquisition time of 2 s (*10*) and fast acquisition times of 1 ms for a bandwidth of 0.5 nm (*11*). However, these methods have yet to demonstrate tens of nanometers of spectral bandwidth at millisecond acquisition times.

The broadband CRDS reported here addresses all of the mentioned system characteristics by efficiently coupling a broadband frequency comb into a high-finesse optical cavity to create the simultaneous ringdown decay of 125,000 individual cavity modes. We report a spectral bandwidth of 100 nm that is limited only by the bandwidth of a mode-locked femtosecond laser. A spectral resolution of 0.8 cm^{-1} was achieved, which can extract linewidths as narrow as 0.01 cm^{-1} (0.3 GHz) via measured pressure broadening of the spectral width of the gas target. An integrated absorption sensitivity of 1×10^{-8} at 1 s was achieved, and an acquisition time of 1.4 ms was realized for a spectral window of more than 15 nm. In principle, this acquisition time is limited only by the actual cavity ringdown time (several microseconds). We present measurements of several atomic and molecular species (Ar, C_2H_2, O_2, H_2O, and NH_3), revealing quantitative information about the gas concentrations, linewidths, collision rates, temperatures, and plasma dynamics.

Broadband CRDS differs from previously demonstrated CRDS methods in how the broadband frequency comb is coupled to the ringdown cavity and the way in which broadband ringdown events are detected. In general, CRDS is performed by overlapping the laser frequency to that of a cavity resonance, allowing light to couple into the cavity, with the resulting ringdown curve providing absorption information at the laser wavelength. In the broadband comb case, we simultaneously couple 125,000 comb components to their respective longitudinal cavity modes and subsequently provide separate detections of ringdown waveforms available from many parallel channels in a single transmitted beam.

In principle, the frequency comb and the cavity are a natural match. The regularly spaced resonant frequency structure of the comb provides the potential for coupling the entire incident power into the cavity over a large spectral bandwidth. In practice, such coupling is difficult to achieve. The frequency structure of the comb is given by the relation $\nu_n = nf_{rep} + f_o$, where the integer n refers to the nth mode of the comb and f_{rep} and f_o refer to the repetition frequency and the carrier-offset frequency, respectively (*12*). To match this set of frequencies to a specific, regularly spaced set of cavity modes, both f_{rep} and f_o must be independently controlled (*13*). For the titanium-doped sapphire (Ti:sapphire) oscillator we used, such control was achieved with several piezo-electric (PZT) and picomotor actuators that adjusted the length and dispersion of the laser cavity. f_{rep} was controlled by adjusting the cavity length by using a combination of a picomotor for coarse adjustments and a PZT for fine adjustments. This combination can precisely adjust f_{rep} by as much as 4 MHz. We controlled f_o by tilting the high-reflecting mirror in the dispersive arm of the Ti:sapphire laser (*14*). This mirror is mounted on two PZTs that are actuated simultaneously to rotate the mirror by a fraction of a degree ($\pm 2 \times 10^{-4}$). Rotating this mirror causes a differential change in the phase and group velocities of the light inside of the laser cavity, which can tune the value of f_o across its entire range from zero to f_{rep}. When the comb frequencies are matched to the cavity modes, successive laser pulses add coherently inside of the cavity, which enhances intracavity intensities and ringdown signals.

Independent control of both degrees of freedom of the comb is only half of the solution to the problem of coupling the comb to the cavity over a large spectral bandwidth. Dispersion in an optical cavity causes the cavity modes to be spaced nonuniformly, producing a cavity resonant frequency structure that the comb cannot match rigorously. All of the optical elements, including the intracavity gases under investigation, have dispersive properties that tend to make the cavity mode spacing nonuniform. Thus, we needed to construct a ringdown cavity that has the appropriate dispersion properties by using low-dispersion, broadband mirrors, and, depending on the gas pressure under investigation, a negative-dispersion mirror to compensate for the positive material dispersion introduced by the gas (*15*). The high cavity finesse for enhanced detection sensitivities must be balanced with usable spectral bandwidth that can be coupled into the cavity for a given property of mirror dispersion. Higher reflectivity mirrors can provide a longer ringdown signal that leads to more sensitive detection, but they also reduce the cavity linewidth, such that a smaller amount of uncompensated dispersion will limit the bandwidth of the comb that can

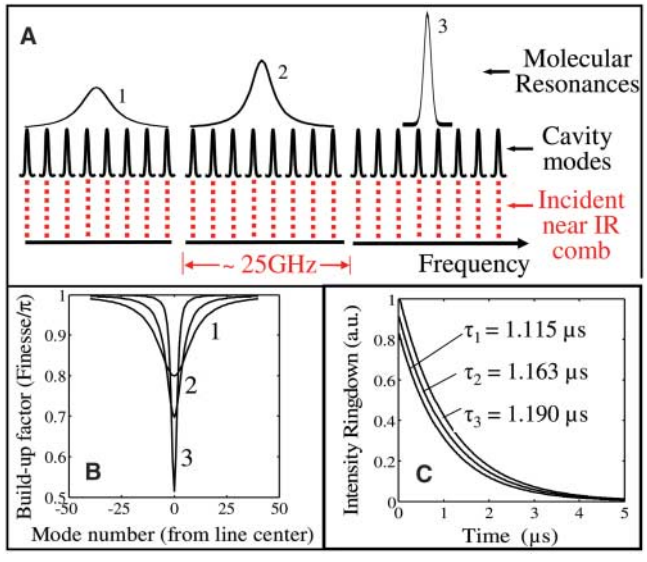

Fig. 1. **(A)** A frequency-domain schematic of the interaction between the femtosecond laser modes, the cavity modes, and the molecular resonances. The set of laser/cavity modes associated with each molecular resonance represents the detection window of 25 GHz set by the monochromator resolution. Each detection window contains roughly 60 cavity modes that ring down simultaneously onto a single detector. **(B)** The calculated buildup of individual cavity modes for three different molecular resonances shown in (A). The buildup is normalized against F/π, the maximum cavity buildup. **(C)** The calculated ringdown signals for the buildup profiles in (B) show that broader absorption peaks result in overall less buildup and shorter ringdown times. a.u., arbitrary units.

be coupled into the cavity. We used mirrors with reflectivity >0.999 between 790 and 850 nm that maintained the cavity dispersion at <10 fs², which allowed for the simultaneous coupling of the comb components into the cavity over this entire wavelength range. Outside of this wavelength range, the nonuniform structure of the cavity modes limits the single-shot detection bandwidth, although it never falls below 15 nm over the entire laser spectrum.

For detection, the resolving power of current dispersive systems—such as a grating monochromator—is not high enough to resolve individual modes of the frequency comb. Each detector element is actually recording the combined ringdown of several cavity modes. The time-varying intensity of the combined ringdown signal is a sum of individual cavity mode ringdown signals incident on a single detector element, $I_{\text{combined}}(t) = \sum_i I_i e^{-\kappa_i t}$. Here I_i and κ_i are the intracavity built-up intensity and the inverse decay time for the ith cavity mode, respectively, I_{combined} is the signal recorded by the detector, and t is time. For the ¼-m monochromator we used, each detector element captured ~60 comb modes, which corresponds to a resolution of 25 GHz. This combination of many ringdown decay signals onto a single detector can be exploited to extract information about the line shape of molecular resonances from the recorded decay time. A simulation of how the ringdown time recorded by a detector element changes for three different molecular resonance line shapes, all with the same absorption strength, is shown in Fig. 1. A detailed model of the ringdown system was created that included cavity buildup affected by the intracavity absorption, ringdown time, the line shape and transition strength of the molecular resonance, and filtering effects of the monochromator.

By using this model, we calculated and compared the ringdown signal due to a molecular resonance of fixed transition strength and three different Lorentzian linewidths (Fig. 1A). Each of the three graphical windows represents a single detector element containing 60 comb modes and a single molecular resonance. The three molecular resonances differ only by the amount of homogeneous broadening included in their respective Voigt line shapes. The total area under each of these resonances is fixed, corresponding to constant absorption strength. The calculated buildup of intracavity light intensity versus cavity mode for each molecular resonance (Fig. 1B) assumes perfect coupling of the comb modes to their respective cavity modes in the absence of absorption.

These simulations show that the broad resonance 1 results in less intracavity buildup intensity and a faster ringdown time, whereas the narrow resonance 3 yields more buildup and a longer ringdown time (Fig. 1C). This effect depends on the number of cavity modes that interact with the molecular absorption and the strength of the interaction. For resonance 3, only a few cavity modes interact with a strong molecular absorption, causing these modes to build up much less and ring down much faster than the majority of other modes inside the detector window. Hence, the contribution of the interacting modes to the overall ringdown signal is small in amplitude and decays away quickly relative to the noninteracting modes. In contrast, resonance 1 allows many modes to interact with the same molecular absorption feature. Here the buildup and ringdown of the interacting modes is not diminished as much relative to the noninteracting modes. Thus, a large contribution to the overall ringdown signal was made by modes that interacted with the molecular absorption.

This type of analysis allows for the determination of the linewidth of a resonance with a resolution much higher than the actual resolving power of the spectrometer. This same analysis can be used to determine the transition strength of molecular transitions by varying the concentration of the gas sample. Finally, if both the transition strength and linewidth for a particular resonance are unknown, they can be determined by using this method of studying the ringdown signal under various target gas concentrations and buffer gas pressures.

For the experimental setup, we used a mode-locked Ti:sapphire laser that generates a train of ~10-fs pulses with a repetition frequency (f_{rep}) of 380 MHz and an average power of 300 mW. This femtosecond optical frequency comb was

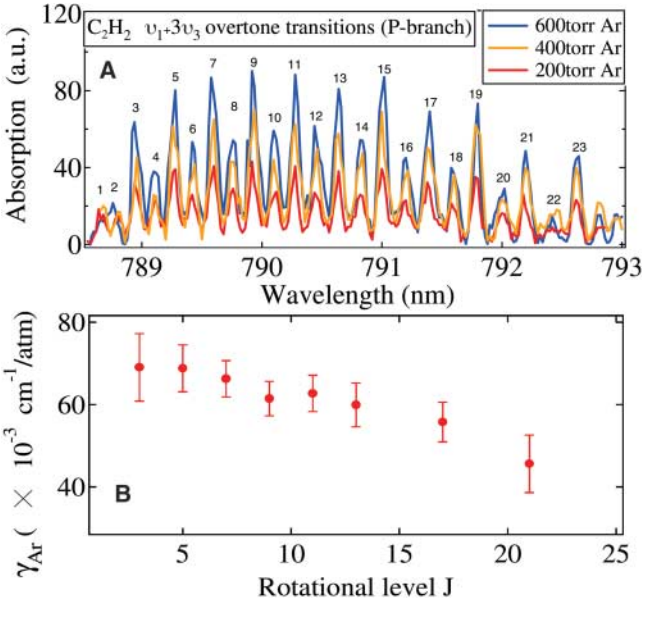

Fig. 2. (**A**) An average of 1000 scans of the P-branch spectrum of the $\upsilon_1 + 3\upsilon_3$ overtone band of C_2H_2. The rotational quantum number for the ground state of each transition is indicated above the spectral peak. The three traces show the change in spectral intensity under a fixed C_2H_2 pressure and three different argon pressures. (**B**) The measured half width at half maximum pressure broadening coefficients (cm^{-1}/atm) for several rotational lines show a decreasing collision rate with increasing rotational quantum number J. Error bars indicate the uncertainty in line shape fit and gas pressures.

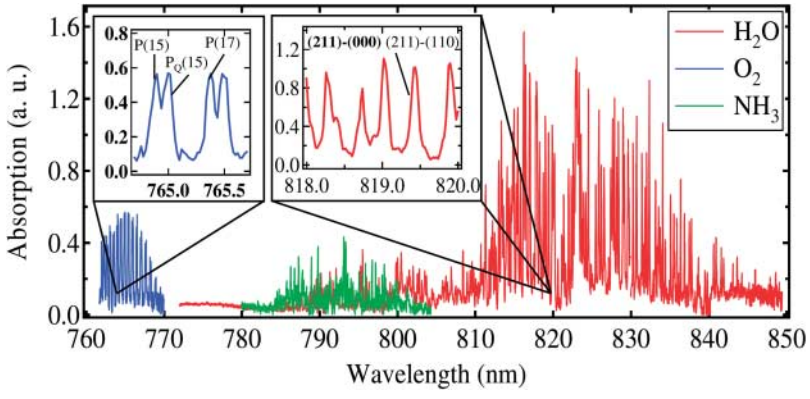

Fig. 3. The overtone spectrum of H_2O (red), the P-branch of the (0,0) vibrational transition of the $^{X3}\Sigma_g^- \rightarrow {}^{b1}\Sigma_g^+$ electronic transition in O_2 (blue), and the overtone spectrum of NH_3 near 790 nm (green) demonstrate the broadband, high-resolution, and high-sensitivity capabilities of this spectroscopic technique. For each molecule, 1000 spectral scans were averaged to produce the traces shown. The inset graphs show that the individual rotational lines of each spectrum have been resolved, revealing the characteristic doublet structure of the O_2 rotational spectrum and the irregular structure of the H_2O rovibrational spectrum. Three of the P-branch lines of O_2 and one H_2O line are labeled. For the H_2O line, the bold text labels the excited and ground vibrational states, and the normal text labels the excited and ground rotational states, respectively.

passed through an acousto-optical modulator (AOM), and the first order diffraction from the AOM (~150 mW) was coupled into a high finesse (F = 4500) optical cavity where the ringdown spectroscopy was performed (*16*). The free spectral range (FSR) of the cavity was 380 MHz, which matches that of the optical comb. With the AOM switched on and the comb components tuned to resonate with respective cavity modes, thousands of femtosecond pulses coherently add inside of the cavity. When the light inside of the cavity reached a preset intensity, the AOM was switched off and the intensity in each cavity mode began to decay (ring down). Light transmitted from the cavity (>50% of the total incident power) was passed through a ¼-m monochromator with a spectral resolution of 25 GHz. The detection of ringdown events was performed by a detector placed at the monochromator output image plane. In cases where fast, broadband spectral acquisition was desirable, a streak camera detection scheme was used (*17*). A scanning mirror was placed near the output image plane of the monochromator and was used to deflect the beam in the vertical direction. Spectrally dispersed wavelengths were recorded along the horizontal rows of pixels, whereas the ringdown waveform in the time domain was recorded on the vertical columns of pixels. The scanning mirror was operated at 355 Hz, allowing for the acquisition of a ringdown spectrum every 1.4 ms. The charge-coupled device (CCD) had 340 pixels in the horizontal dimension, allowing for a single-shot acquisition of 15 nm of spectrum at 25-GHz resolution.

The first molecular sample we studied with this system was acetylene (C_2H_2). The linear rotor structure of C_2H_2 results in a relatively simple spectrum (Fig. 2A). The transitions in the $\upsilon_1 + 3\upsilon_3$ overtone band originate from rotational levels in the vibrational ground state and are excited to the $\upsilon_1 = 1$, $\upsilon_3 = 3$ overtone band and $\Delta J = -1$ states (P-branch). The relative strengths of these transitions are described by a Boltzmann distribution $S_J \propto Jg_i e^{-E_J/k_BT}$, where J is the rotational quantum number, g_i is the nuclear spin degeneracy, E_J is the energy of the Jth rotational level in the vibrational ground state, and k_BT indicates the thermal energy of the gas (*18*). The nuclear spin dependence arises from the fermionic nature of C_2H_2. As a result, symmetric spin states must be paired with antisymmetric rotational states and vice versa. Symmetric (ortho) spin states outnumber the antisymmetric spin states (para) by a ratio of 3:1, and the relative strengths of adjacent rotational transitions are similarly weighted.

A fixed C_2H_2 pressure (2 torr) at fixed temperature (295 K) was maintained inside the ringdown cavity, and spectra were recorded while the pressure of an inert buffer gas (argon) was varied between 200 and 600 torr. Collisions between argon and C_2H_2 increased the Lorentzian contribution to the Voigt line shape of the C_2H_2 resonances, and this Lorentzian broadening of the C_2H_2 resonances was detected as a decrease in the cavity ringdown time that results from the larger number of comb modes interacting with the molecular absorption (Fig. 2A). Changes in the Lorentzian linewidth as small as 200 MHz can be detected in this way, providing resolution that is two orders of magnitude better than that of the monochromator. The pressure broadening rate of the Lorentzian linewidth was linear in pressure. The half width at half maximum pressure broadening coefficients were plotted as a function of rotational level J (Fig. 2B). The measured pressure broadening coefficients for the P-branch of the $\upsilon_1 + 3\upsilon_3$ overtone of C_2H_2 are in good agreement with measurements by Herregodts *et al*. (*19*), which used continuous wave (CW) absorption techniques that required much more challenging frequency-referencing methods to achieve a similar level of precision.

The second molecule we examined was water (H_2O). Between 780 and 850 nm, H_2O has an enormous number of transitions corresponding to several vibrational modes and hundreds of rotational levels. Because of its complicated asymmetric top structure, the H_2O spectrum has a highly irregular structure. However, this large range of transition frequencies makes it an ideal candidate to demonstrate the broadband and yet high-resolution characteristics of this method. The H_2O spectrum was measured from 100 mtorr to 20 torr (relative humidities ranging from 0.5 to 90%). Both absolute pressure and partial pressure (mixed with argon) measurements were performed within this pressure range. The H_2O overtone spectrum between 770 and 850 nm is shown in Fig. 3 for 10 torr of H_2O and 600 torr of argon buffer gas. The inset identifies the rovibrational transition: (000) to (211) in vibrational quantum numbers (ν_1, ν_2, ν_3) and (110) to (211) in rotational quantum numbers (J, k_a, k_c) (*20*).

To demonstrate fully the broadband nature of this system using the entire spectral bandwidth of the laser, the spectrum of an electric dipole forbidden electronic transition in $O_2({}^{X3}\Sigma_g^- \rightarrow {}^{b1}\Sigma_g^+)$, where X indicates the electronic ground state, g (gerade) indicates even symmetry, and b indicates the excited electronic state. Overtone transitions of NH_3 were also detected, and the rotational lines were identified. For the O_2 measurement, the cavity was filled with 600 torr of air corresponding to a pressure of 124.8 torr of O_2. For the NH_3 data, a partial pressure of 3 torr was used. Together, the H_2O, NH_3, and O_2 spectra presented in Fig. 3 demonstrate nearly the entire 100-nm spectral width that can be probed simultaneously with the current frequency comb–cavity system.

The final two measurements presented here aim to demonstrate the fast spectral acquisition time of this system. First, a single-shot measurement of the H_2O spectrum was used to demonstrate the current limit on the spectral acquisition

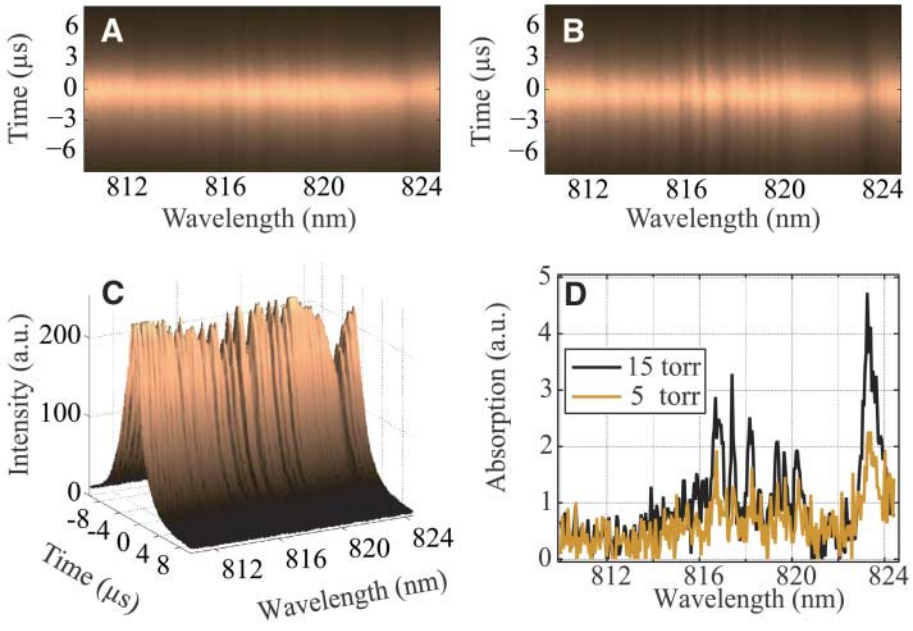

Fig. 4. Fast spectral acquisition provided by broadband CRDS. A portion of the H_2O overtone spectrum near 820 nm recorded with (**A**) 5 torr and (**B**) 15 torr of H_2O, containing 15 nm of spectral information, was acquired by the camera in 30 μs and transferred to the computer. For these plots, t = 0 corresponds to the time when the AOM is shut off. For $t < 0$, the cavity is building up, and for $t > 0$ the cavity is ringing down. (**C**) A surface plot of the 15-torr image shows a reduction in cavity buildup and more rapid cavity decay in spectral regions corresponding to H_2O absorption. (**D**) Decay constants extracted from the 5- and 15-torr images reveal the H_2O absorption spectrum.

time. A second measurement was performed on discharged argon to demonstrate the fundamental limitation to the spectral acquisition time.

The H_2O measurement was performed by recording single ringdown events without averaging. False-color CCD images of two of these single-shot ringdown events were recorded (Fig. 4, A and B) along with the processed data following the procedure described in (*16*). The surface plot (Fig. 4C) shows that high resolution and a broad detection bandwidth were achieved in real time. The noise associated with this detection scheme allows for the detection of changes in integrated absorption (αL, where α is the absorption per unit length and L is the cavity length) of 2.5×10^{-5} using an integration time constant of 0.15 μs per CCD pixel. This corresponds to a detection sensitivity of 1×10^{-8} integrated absorption at 1-s averaging time. The 1.4-ms acquisition time is currently limited by the speed of the optical scanner. The fundamental time limitation for the acquisition of a ringdown spectrum is the cavity lifetime, which is on the order of a few microseconds.

The second real-time measurement, which was performed on a decaying argon plasma, demonstrated a measurement time scale approaching the cavity decay limit. A radio frequency (RF) discharge was used to create argon plasma inside of the ringdown cavity (*21*). The RF source driving the plasma was rapidly switched, and a transition at 811.53 nm (Fig. 5, inset), originating from an argon metastable state $3s^2 3p^5 \left(^2P^0_{3/2}\right)4s \rightarrow 3s^2 3p^5 \left(^2P^0_{3/2}\right)4p$, was studied. Here, the $3s^2 3p^5 \left(^2P^0_{3/2}\right)4s$ is a metastable state with a lifetime >1 s. However, at high temperatures inside the plasma, the metastable argon atoms decay via collisions with the walls of the optical cavity on the order of 10 μs.

When the RF discharge is turned off (at t = 0 μs in Fig. 5), the excited dipole-allowed transitions quickly decay, whereas the metastable atoms decay more slowly. Initially, we observed this effect when a high-pressure argon discharge (4 torr) was established inside the cavity and a collection lens and fast photodiode were placed along side the plasma. The RF discharge was turned off and the spectrally unresolved plasma decay was observed in fluorescence (Fig. 5, red trace), revealing a fast initial decay followed by the slower decay of the metastable states.

The argon plasma pressure was then decreased to 100 mtorr (below the detection capabilities of the fluorescence measurement), and a cavity-based measurement was performed. Because the 811.53-nm transition is strong, a simple cavity transmission measurement was used to measure the decay of the $3s^2 3p^5 \left(^2P^0_{3/2}\right)4s$ state inside of the cavity. The sensitivity of the ringdown cavity is such that 100 mtorr of discharged argon was sufficient to reduce the cavity buildup to 5% of the empty cavity value. The blue dots (Fig. 5) show the intracavity absorption in the presence of metastable argon at 811.53 nm for various times before and after the RF discharge was turned off. The agreement in decay times recorded by the photodiode and the cavity measurement confirms that the long-lived decay seen by the photodiode is indeed due to the decay of the metastable states. The decay time of the metastable state was around 10 μs, whereas the cavity buildup and ringdown times were on the order of 3 μs. This experiment demonstrates that as spectral acquisition times approach the fundamental cavity decay limit, measurements of this type will be performed in a single shot.

A number of improvements can still be implemented to push the system performance to the fundamental limits. With higher resolution detection and by using the latest mirror technology, detection sensitivities of 10^{-10} at 1 s can easily be achieved. The use of state-of-the-art mirrors that are more broadband and less dispersive also implies larger spectral bandwidths, up to several hundred nanometers. Mode-locked laser sources and detectors at spectrally important regions such as 1.5 μm are abundant. A larger (2 m) monochromator, although not an elegant solution, could bring the system resolution to a few gigahertz, and the comb structure would still allow for the investigation of linewidths on the 100s of MHz scale. A virtually-imaged phase array (VIPA) device (*16*) provides an even more attractive option (*22*). Achieving resolutions of <1 GHz, these devices are very close to resolving individual comb modes. Once single–comb mode resolution is realized, the resolution of the system will be limited by the laser or cavity linewidths, which can be made very narrow. Finally, the use of diode array detection eliminates the need for fast scanning optics and data transfer, and it allows acquisition times to approach the fundamental cavity decay limit for the entire spectral bandwidth.

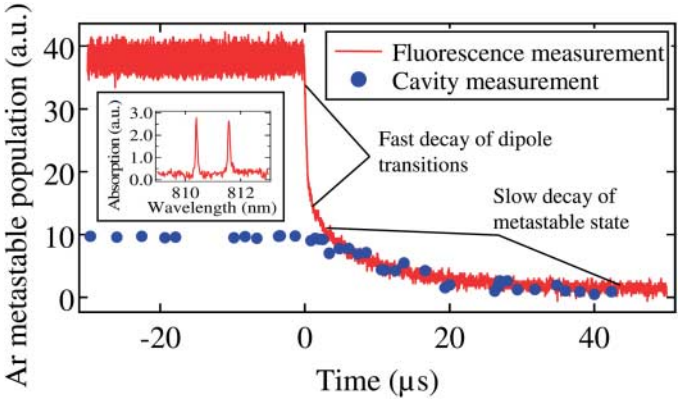

Fig. 5. Decay of hot metastable argon atoms inside of the ringdown cavity is measured by a high–plasma pressure (4 torr) fluorescence measurement and a low-pressure (100 mtorr) cavity transmission measurement. The cavity measurement has been scaled to overlap the fluorescence measurement to highlight the agreement in decay time. The decay time for the hot metastable argon is measured to be 10 μs by both methods. This measurement demonstrates that when the spectral acquisition time of CRDS is reduced to its fundamental limit, measurements such as the hot argon metastable decay will be made with high sensitivity and in a single shot.

References and Notes

1. L. R. Narasimhan, W. Goodman, C. K. N. Patel, *Proc. Natl. Acad. Sci. U.S.A.* **98**, 4617 (2001).
2. S. A. Kharitonov, P. J. Barnes, *Am. J. Respir. Crit. Care Med.* **163**, 1693 (2001).
3. F. Keilmann, C. Gohle, R. Holzwarth, *Opt. Lett.* **29**, 1542 (2004).
4. S. T. Sanders *et al.*, *Opt. Photonics News* **16**, 36 (2005).
5. J. Ye, L. S. Ma, J. L. Hall, *Opt. Lett.* **21**, 1000 (1996).
6. J. Ye, L. S. Ma, J. L. Hall, *J. Opt. Soc. Am. B* **15**, 6 (1998).
7. J. Ye, J. L. Hall, *Phys. Rev. A.* **61**, 061802 (2000).
8. T. Gherman, D. Romanini, *Opt. Express* **10**, 1033 (2002).
9. E. R. Crosson *et al.*, *Rev. Sci. Instrum.* **70**, 4 (1999).
10. Y. He, B. J. Orr, *Appl. Phys. B* **79**, 941 (2004).
11. I. Debecker, A. K. Mohamed, D. Romanini, *Opt. Express* **13**, 2906 (2005).
12. S. T. Cundiff, J. Ye, *Rev. Mod. Phys.* **75**, 325 (2003).
13. R. J. Jones, I. Thomann, J. Ye, *Phys. Rev. A.* **69**, 051803 (2004).
14. J. Reichert, R. Holzwarth, T. Udem, T. W. Hänsch, *Opt. Commun.* **172**, 59 (1999).
15. M. J. Thorpe, R. J. Jones, K. D. Moll, J. Ye, R. Lalezari, *Opt. Express* **13**, 882 (2005).
16. Materials and methods are available as supporting material on *Science* Online.
17. J. J. Scherer *et al.*, *Appl. Opt.* **40**, 6725 (2001).
18. J. Ye, thesis, University of Colorado (1997).
19. F. Herregodts, D. Hurtmans, J. Vander Auwera, M. Herman, *Chem. Phys. Lett.* **316**, 460 (2000).
20. High-resolution transmission (HITRAN) molecular database, 2005.
21. C. I. Sukenik, H. C. Busch, *Rev. Sci. Instrum.* **73**, 493 (2001).
22. A. Vega, A. M. Weiner, C. Lin, *Appl. Opt.* **42**, 4152 (2003).

23. We thank E. Hudson for technical discussions and S. Cundiff, H. Lewandowski, and R. McLeod for equipment loans. The research work at JILA is supported by Air Force Office of Scientific Research, the Office of Naval Research, NASA, NIST, and NSF. M.J.T. thanks NSF–Integrative Graduate Education and Research Traineeship Program and the University of Colorado Optical Science and Engineering Program for financial support. J.Y. is a member of the NIST Quantum Physics Division.

Supporting Online Material

www.sciencemag.org/cgi/content/full/311/5767/1595/DC1
Materials and Methods
Fig. S1
References

15 December 2005; accepted 8 February 2006
10.1126/science.1123921